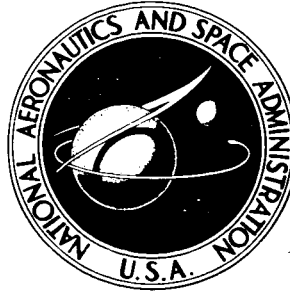


NASA TECHNICAL NOTE

NASA TN D-2182

27p.



OTS: \$

(NASA TN D-2182)

N64-17158*
CODE-1

**INDUCED PRESSURES AND
SHOCK SHAPES ON BLUNT CONES
IN HYPERSONIC FLOW**

by Richard D. Wagner, Jr., and Ralph Watson

*Langley Research Center
Langley Station, Hampton, Va.*

reg
ja

INDUCED PRESSURES AND SHOCK SHAPES ON
BLUNT CONES IN HYPERSONIC FLOW

By Richard D. Wagner, Jr., and Ralph Watson

Langley Research Center
Langley Station, Hampton, Va.

NATIONAL AERONAUTICS AND SPACE ADMINISTRATION

For sale by the Office of Technical Services, Department of Commerce,
Washington, D.C. 20230 -- Price \$0.75

INDUCED PRESSURES AND SHOCK SHAPES ON

BLUNT CONES IN HYPERSONIC FLOW

By Richard D. Wagner, Jr., and Ralph Watson

SUMMARY

17158 A

Numerical solutions and experimental pressure distributions have been studied with the intention of evaluating proposed extensions to the case of blunt cones of the blast-wave correlation of induced pressures. The numerical inviscid solutions obtained by characteristics theory do, with some success, correlate in terms of what may be considered as modified blast-wave parameters. The correlation of experimental pressures, though not as successful as that for the inviscid numerical solutions, is reasonably good. A secondary study of Reynolds number effects indicates that the poorer correlation of the experimental pressures is due, in part, to viscous effects.

The experimental shock shapes are also obtained and found to give a good correlation for small cone angles in terms of blast-wave-type parameters, but the correlation deteriorates for cone semivertex angles near 20° and above. Much of the success here is, however, implied by previous blast-wave correlations of shock shapes on blunt cylinders together with the limited independence of after-body geometry in the shock shape.

Author

INTRODUCTION

Recent theoretical analyses have indicated that through an appropriate modification the blast-wave parameters may be extended to the correlation of induced pressures on blunt cones and wedges. (See refs. 1 to 3.) In reference 4, an analysis of exact inviscid pressures on blunt plates with incidence confirms the extension for the two-dimensional problem by a successful correlation of surface pressures with modified blast-wave parameters. For the blunt cone, the proposed extensions have only recently begun to be scrutinized.

In the present paper an analytical and experimental study of the induced pressures and shock shapes of blunt cones is presented. The analytical study consists of an examination of proposed induced-pressure correlations of exact solutions for blunt cones by blast-wave-type parameters. The experimental study was conducted in the Langley 22-inch helium tunnel. Pressure distribution and shock shapes on six conical afterbodies, having semivertex angles of 2° , 4° , 6° , 10° , 20° , and 30° , were obtained at a free-stream Mach number of 19.4 and with different degrees of nose tip bluntness. Included in the experimental program is a secondary study of the dependence of induced pressure upon Reynolds number.

SYMBOLS

$C_{D,n}$	nose drag coefficient
C_p	pressure coefficient, $\frac{2}{\gamma M_\infty^2} \left(\frac{p}{p_\infty} - 1 \right)$
d_b	aftercone base diameter (sketch a)
d_n	forecone base diameter (sketch a)
L	aftercone length (sketch a)
M_∞	free-stream Mach number
p	static pressure
p_∞	free-stream static pressure
$R_{d,\infty}$	free-stream Reynolds number based on d_n
x_n	model axial coordinate measured from nose tip
x_s	model axial coordinate measured from forecone-aftercone junction
y	shock displacement from axis of symmetry
γ	ratio of specific heats
δ_b	aftercone semivertex angle (sketch a)
δ_n	forecone semivertex angle (sketch a)

APPARATUS AND TEST CONDITIONS

Tunnel

The experimental part of the present investigation was conducted in the Langley 22-inch helium tunnel. This tunnel, a short description of which may be found in reference 5, is an intermittent closed-cycle facility operating in the stagnation pressure range from about 500 to 3,000 psig at ambient temperature. For the present tests, a contoured nozzle, designed to yield a uniform test-section Mach number, was used. Even though the longitudinal Mach number gradient in the test section of this nozzle is negligibly small, a slight variation of Mach number with stagnation pressure is observed. In most cases the tests were conducted at a stagnation pressure of 1,000 psig with a free-stream Mach number

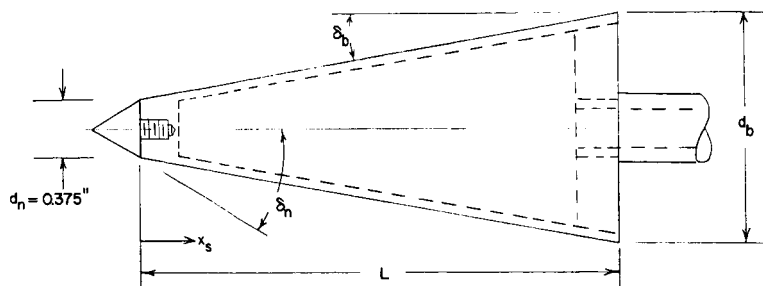
of 19.4 at the model nose location. In a secondary study of Reynolds number effects, the free-stream Mach number variation between tests at different stagnation pressures was $18.9 \leq M_\infty \leq 19.4$ with the corresponding Reynolds number variation of $0.0464 \times 10^6 \leq R_{d,\infty} \leq 0.149 \times 10^6$.

Models

The models used consisted of six conical afterbodies, each tested with three separate nose tips of different degrees of bluntness. The six cones (referred to herein as the aftercones) had semivertex angles of 2° , 4° , 6° , 10° , 20° , and 30° . The nose tips chosen (referred to as the forecones) had semivertex angles of 90° , 46° , and 30° ; the nose drag coefficients of the three forecones, obtained by the modified Newtonian theory and cone theory, are approximately 1.76, 1.16, and 0.56, respectively.

The construction of the basic configuration is shown in sketch a. The overall dimensions of the different models are as follows:

δ_b , deg	L, in.	d_b , in.	$\frac{L}{d_n}$
2	15.00	1.42	40.00
4	15.00	2.47	40.00
6	15.00	3.53	40.00
10	9.40	3.98	25.10
20	3.75	3.11	10.00
30	2.63	3.41	7.02



Sketch a.

The forecones were removable so that each aftercone could be tested with each of the three forecone tips. Each aftercone was instrumented with 0.060-inch-diameter pressure orifices located at the positions given in table I. The pressure gages and test techniques described in reference 5 were used in the present tests.

TABLE I.- ORIFICE LOCATIONS

x_s/d_n for -					
$\delta_b = 2^\circ$	$\delta_b = 4^\circ$	$\delta_b = 6^\circ$	$\delta_b = 10^\circ$	$\delta_b = 20^\circ$	$\delta_b = 30^\circ$
1.03	0.96	0.89	0.84	0.39	0.40
2.05	1.97	1.90	1.80	.58	.60
3.03	2.97	2.88	2.78	.97	.81
4.01	3.95	3.85	3.75	1.41	1.02
4.99	4.96	4.88	4.76	1.97	1.41
5.99	5.96	5.90	5.70	2.52	1.80
7.89	7.96	7.87	7.64	2.97	2.41
9.72	9.93	9.86	9.59	3.52	3.25
13.00	12.90	12.80	12.50	4.53	4.01
17.00	16.90	16.80	16.40	5.52	4.99
20.00	19.90	19.80	19.30	7.03	
24.80	24.90	24.70	21.90	8.29	
29.70	29.90	27.00			
35.00	34.90	34.70			

RESULTS

Numerical Solutions

Exact inviscid pressure distributions were obtained for configurations having aftercones with semivertex angles ranging from 2° to 20° and having different degrees of nose tip bluntness.

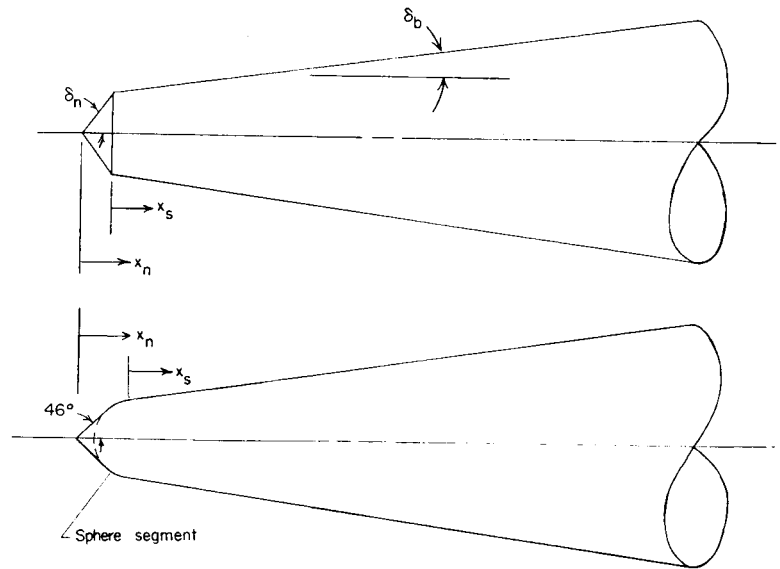
The configurations studied are shown in sketch b. In most cases the nose tips chosen were forecones, as with the models of the experimental program, with semivertex angles of 46° , 30° , and 20° ($C_{D,n} \approx 1.16$, 0.56 , and 0.25),

but some calculations were made for a spherical nose tip capped by a near sonic cone ($C_{D,n} \approx 0.8$). Inasmuch as the

entire flow fields were supersonic with these nose tips, the axisymmetric, rotational characteristics method of reference 6 could be used. The

calculations were made on the IBM 704 electronic data processing machine and employed the program developed for the

study reported in reference 7. Calculations were made for both helium ($\gamma = 5/3$) and air ($\gamma = 7/5$). Most of the results were obtained at free-stream Mach numbers near 20; however, some results were obtained at free-stream Mach numbers near 10 and 40.



Sketch b.

In order to illustrate the essential features of the pressure distribution over the blunt cone, some results for $\gamma = 5/3$ and the 30° forecone are shown in figure 1. The pressure distributions are in the form of a ratio of surface static pressure to free-stream static pressure plotted against the nondimensional axial distance x_n/d_n . The distributions for the models with the various aftercone angles display the common feature of a pressure decay region in which an overexpansion occurs and is followed by a recompression. Obviously, the pressures far downstream should asymptotically approach the sharp-cone pressure values indicated in the figure. These values are as given by sharp-cone theory.

Recent theoretical analyses employing hypersonic slender-body theory or blast-wave analogies have produced blast-wave-type parameters for correlating induced pressures and shock shapes on slender blunt cones. (See refs. 1 to 3.) In the prediction of inviscid flow-field properties on blunt cylinders, the concepts given by the blast-wave theory are quite useful. (See ref. 7, for example.) Although the induced pressures on blunt cylinders may be significantly influenced

by finite viscosity (see ref. 5), inviscid solutions usually serve as starting points for complete analysis of flow fields. For this reason, among others, the evaluation of proposed blast-wave extensions to blunt cones by examination of the inviscid numerical solutions would be of considerable interest.

The results of the numerical calculations for $\gamma = 5/3$ are shown in figure 2. (The calculations for $\gamma = 7/5$ are discussed subsequently.) The characteristics solutions (represented by the symbols) are presented in terms of the correlating parameters developed by Cheng in reference 2. The sharp-cone values for $M_\infty = 20$ are also indicated in the figure, along with Cheng's theoretical correlation curve. As in the blast-wave theory, the correlation should not apply in the immediate vicinity of the nose. With this exception, the data fall within a band. In the region of the overexpansion, the characteristics solutions give higher values of induced pressures than Cheng's theory and the correlation becomes poorer than in the region of the pressure decay. In the analysis of reference 2, the form of the Newtonian-plus-centrifugal-force pressure dependence adopted implies large pressure ratios which would limit the results accordingly. For the small-angle aftercone, a downstream limit for good correlation should then be expected. This is apparent in the seemingly poor correlation in the region of the overexpansion, and is further illustrated by the unsuccessful correlation of the sharp-cone pressures for small cone angles.

Mirels and Thornton (ref. 3) have also considered the problem of blunted, slender cones and arrive at correlating parameters similar to those of Cheng; the difference being that they find $\frac{C_p}{\delta_b^2}$ (instead of $\frac{2}{\gamma M_\infty^2 \delta_b^2} \frac{p}{p_\infty}$) should be used

as the correlating parameter against the axial-distance parameter $\frac{\delta_b^2}{\sqrt{C_{D,n}}} \frac{x_n}{d_n}$.

Obviously, the parameters of references 2 and 3 are essentially the same for large ratios of local to free-stream static pressure, but the more unifying effect of the parameters used by Mirels and Thornton is demonstrated in figure 3(a) wherein the characteristics solutions are again shown but in terms of the parameters of reference 3. The correlation for all configurations studied, in the area of the overexpansion and including the sharp-cone pressures, is somewhat improved when expressed in terms of the pressure-coefficient parameter. The theoretical distribution of Mirels and Thornton, shown also in figure 3(a), is

restricted to small values of the distance parameter $\frac{\delta_b^2}{\sqrt{C_{D,n}}} \frac{x_n}{d_n}$ (as pointed out

in ref. 3) and lies roughly within the correlation band.

The characteristics solutions are again correlated in figure 3(b). In this figure, the axial distance measured from the forecone-aftercone junction (see x_s in sketch b) has been used in the distance parameter. A slight improvement occurs at the beginning and in the area of the overexpansion. For extreme values of the distance parameter, small and large, no further improvement results. For the most part, the choice of x_s or x_n would be a matter of convenience. It is noteworthy that the induced pressures at $M_\infty \approx 20$ on the 2° aftercone do not

show everywhere good correlation with the other aftercone induced pressures. This result is consistent with the results of Baradell and Bertram who consider the corresponding two-dimensional problem in reference 4. They found by using the parameters suggested in reference 1, which are essentially the same as those of reference 3, that the pressures on blunt wedges did not correlate well below a wedge angle of about 3° .

The results obtained for $\gamma = 7/5$ are shown in figure 4. (In many cases numerical difficulties were introduced by the convergence of characteristics lines reflected from the aftercone surface in a compression region occurring downstream of the forecone-aftercone junction, as, for example, for $0^\circ \leq \delta_b \leq 6^\circ$ in figure 1. These difficulties resulted in a limit to the extent downstream to which the calculations could be made and occurred in the calculations for both specific heat ratios, but especially for $\gamma = 7/5$.) The shaded area superimposed on the data represents the correlated results for $\gamma = 5/3$ for the same aftercone angle range (that is, $\delta_b = 2^\circ$ to 10°). For small values of the distance parameter, the regions of good correlation of the characteristics solutions calculated for helium and air essentially overlap. In addition, there is little difference in the sharp-cone values. It would seem that in this form of correlation, the effects of γ are reduced and are nearly insignificant in a large portion of the induced-pressure region.

Experimental Results

The experimental pressure distributions obtained on the models at $M_\infty = 19.4$ and $R_{d,\infty} = 0.149 \times 10^6$ are plotted in figure 5. Though the data do not extend far enough downstream in most cases to obtain the asymptotic pressures, in all cases except for the 2° and 4° aftercones, the data have the common feature (as in the numerical solution of fig. 1) of an overexpansion followed by a recompression to near sharp-cone pressure. The downstream extent to which tip bluntness affects the pressure distribution is seen to diminish with increasing aftercone angle. A comparison of the two extreme cases of bluntness, $C_{D,n} = 1.76$ and 0.56 ($\delta_n = 90^\circ$ and 30° , respectively), reveals the blast-wave-type feature of a more rapid pressure decay with higher nose drag coefficient.

The downstream pressures on the 2° aftercone seem to indicate the presence of viscous effects when compared with the inviscid sharp-cone pressures. An illustration of the presence of viscous effects and an indication of their magnitude is shown in figure 6 by a comparison of the experimental data with the characteristics solutions with a fixed 30° forecone. The viscous effects are quite large over the induced-pressure region for the small aftercone angles but appear of diminishing importance as the aftercone angle increases. The overexpansions indicated by the exact inviscid solutions are not seen in the data for the 2° and 4° aftercones and are reduced for the larger cone angles.

In view of the preceding results, a secondary study of the effects of Reynolds number variation was performed on the 4° and 6° aftercones with the 90° and 30° forecone tips. In order to cover a wider range of Reynolds number, based on forecone base diameter, the removable nose tips were interchanged with

extensions having forecone base diameter ($3/16$ inch) smaller than that of the basic models, and tests were also made at different stagnation pressures.

In reference to the 90° forecones (see top of fig. 7), above a Reynolds number of about 0.0742×10^6 for both the 4° aftercone and 6° aftercone, the results are consistent with the results of reference 5. In reference 5, it was found during the study of the Reynolds number effects on induced pressures of cylindrical bodies that for high-nose-drag shapes the viscous effects were unimportant in the area of the pressure decay. (The values for $R_{d,\infty}$ in ref. 5 ranged from 0.088×10^6 to 2.65×10^6 .) Nevertheless, the data shown in figure 7 for the lowest value of $R_{d,\infty}$ indicate a rapid transition to a region where viscous effects may become predominant. This is an interesting aspect of the observed effects and warrants further investigation.

Quite different results are obtained on the aftercones with 30° forecone tips. As shown in figure 7, Reynolds number variation produces appreciable effects over the entire aftercone and these effects steadily increase with decreasing $R_{d,\infty}$. Again, this result is in line with the results of reference 5 wherein, for low-nose-drag cylindrical bodies, viscous effects were found important over the entire induced-pressure region.

In view of the preceding discussion, it would appear that correlation of experimental data on blunt cones should take into consideration the effects of Reynolds number. In figure 8 are shown the data on blunt cones obtained at the highest Reynolds number presented in terms of the parameters suggested by Mirels and Thornton (ref. 3), employing the axial distance from the forecone-aftercone junction in the distance parameter. The data are shown for body stations greater than about $x_s/d_n = 2$. Although the correlation is not as good as that for the characteristics solutions, the experimental data do correlate into a band. Notice that in reference to the theoretical correlation curve of reference 3, the experimental correlation band is higher than the characteristics band of correlation in figure 3(b). This observation and the larger bandwidth are indicative of the viscous effects mentioned previously and further point out their importance.

A recent publication has been called to the authors' attention in which a correlation of experimental induced pressures on hemispherically blunted cones, obtained in an arc-driven nitrogen tunnel, is reported. (See ref. 8.) The data

of reference 8 are correlated in terms of the parameters $\frac{C_p}{2\delta_b^2}$ and

$\frac{\delta_b^2}{\sqrt{C_{D,n}}} \frac{x_n}{d_n} \sqrt{\frac{\gamma+1}{\gamma-1}}$. The distance parameter is that developed by Cheng in reference 2 (in fig. 2 of the present paper, the factor containing γ is deleted); the pressure parameter is suggested in reference 8 as a modification of Cheng's pressure parameter. The fact that the correlation band of the data of reference 8 is higher than the present characteristics correlation, for $\gamma = 7/5$ and approximately the same aftercone-angle range, indicates a possible Reynolds number effect on the correlation as in the present experimental data.

In an effort to examine the possibilities of correlating the shock shapes of blunt cones, the shock shapes were measured from the schlieren photographs shown in figure 9. The shock shapes are plotted in figure 10 in terms of the correlating parameters developed in references 2 and 3. (The data are shown only for $x_s/d_n > 1.5$ since, as for the induced pressures, the correlation should not apply too near the nose.) These parameters are essentially the same in references 2 and 3, the difference being that reference 2 includes a function of γ to account for its variation. The shock shapes for the blunt cones with small

aftercone angle correlate well in terms of the parameters $\delta_b \sqrt{\frac{2}{C_{D,n}}} \frac{y}{d_n}$ and

$\frac{\delta_b^2}{\sqrt{C_{D,n}}} \frac{x_n}{d_n}$; though for the 20° and 30° aftercones, the correlation is not quite as good. The sharp-cone shocks which are the asymptotes of the blunt-cone shocks are also given in the figure and are correlated with fair success by these parameters.

The theoretical correlation curves of references 2 and 3 are also given in figure 10. Both Cheng's theory and that of Mirels and Thornton underestimate the shock displacement. Of course, the shock shape of a blunt cone should be identical to the corresponding blunt cylinder up to a point downstream where the afterbody geometry would influence the shock. This feature is exhibited by the near 0.5 power law variation observed in the experimental data and in both theoretical

correlations for $\frac{\delta_b^2}{\sqrt{C_{D,n}}} \frac{x_n}{d_n} < 1.0$ in figure 10. This variation is typical

of the shocks on blunt cylinders. The transition to the conical shock occurs

around $\frac{\delta_b^2}{\sqrt{C_{D,n}}} \frac{x_n}{d_n} = 1.0$. Cheng's theory shows the transition, but Mirels and

Thornton's, which (as they mention) is restricted to small values of the distance parameter, does not.

CONCLUSIONS

On the basis of the results of the present investigation, the following conclusions may be made:

1. Inviscid numerical solutions for the induced pressures on blunted cones may be correlated by the blast-wave-type parameters $\frac{C_p}{\delta_b^2}$ and $\frac{\delta_b^2}{\sqrt{C_{D,n}}} \frac{x_n}{d_n}$ with fair success. In addition, in this form of correlation, the differences between the induced pressures for air and helium seem to be small over a large portion of the region.

2. The results of measurements of experimental induced pressures on blunt cones indicate that Reynolds number variations may significantly affect the

induced pressures. Though the scope of the study of Reynolds number effects was not extensive enough to define these effects clearly, the indications are that at sufficiently high Reynolds number the effects are small for the high-nose-drag blunt cones but that there is a rapid transition to a region of large viscous effects at low Reynolds numbers. The effects were significant for low-nose-drag blunt cones throughout the Reynolds number range of the tests.

3. Experimental pressures at the highest test Reynolds number were found to correlate into a band in terms of the preceding blast-wave-type parameters. The correlation was not as successful as for the inviscid numerical solutions and this poor correlation is attributed to the viscous effects.

4. The experimental shock shapes show good correlation in terms of the parameters $\delta_b \sqrt{\frac{2}{C_{D,n}}} \frac{y}{d_n}$ and $\frac{\delta_b^2}{\sqrt{C_{D,n}}} \frac{x_n}{d_n}$; though for the 20° and 30° aftercones, the correlation is not quite as good. For the blunt cones with small aftercone angle, the success of the correlation is due to independence (of the forward part of the shock) of afterbody geometry and represents merely a further confirmation of the blast-wave correlation of shock shapes.

(The symbols used in the blast-wave-type parameters are defined as follows: C_p , pressure coefficient; δ_b , aftercone semivertex angle; $C_{D,n}$, nose drag coefficient; x_n , axial distance from nose tip; d_n , forecone base diameter; and y , shock displacement from axis of symmetry.)

Langley Research Center,
National Aeronautics and Space Administration,
Langley Station, Hampton, Va., October 23, 1963.

REFERENCES

1. Chernyi, G. G.: Effect of Slight Blunting of Leading Edge of an Immersed Body on the Flow Around It at Hypersonic Speeds. NASA TT F-35, 1960.
2. Cheng, Hsien K.: Hypersonic Flow With Combined Leading-Edge Bluntness and Boundary-Layer Displacement Effect. Rep. No. AF-1285-A-4 (Contract Nonr-2653(00)), Cornell Aero. Lab., Inc., Aug. 1960.
3. Mirels, Harold, and Thornton, Philip R.: Effect of Body Perturbations on Hypersonic Flow Over Slender Power Law Bodies. NASA TR R-45, 1959.
4. Baradell, Donald L., and Bertram, Mitchel H.: The Blunt Plate in Hypersonic Flow. NASA TN D-408, 1960.
5. Wagner, Richard D., Jr., and Watson, Ralph: Reynolds Number Effects on the Induced Pressures of Cylindrical Bodies With Different Nose Shapes and Nose Drag Coefficients in Helium at a Mach Number of 24. NASA TR R-182, 1963.
6. Ferri, Antonio: Elements of Aerodynamics of Supersonic Flows. The Macmillan Co., 1949.
7. Van Hise, Vernon: Analytic Study of Induced Pressure on Long Bodies of Revolution With Varying Nose Bluntness at Hypersonic Speeds. NASA TR R-78, 1961.
8. Griffith, B. J., and Lewis, Clark H.: A Study of Laminar Heat Transfer to Spherically Blunted Cones and Hemisphere-Cylinders at Hypersonic Conditions. AEDC-TDR-63-102 (Contract No. AF 40(600)-1000), Arnold Eng. Dev. Center, June 1963.

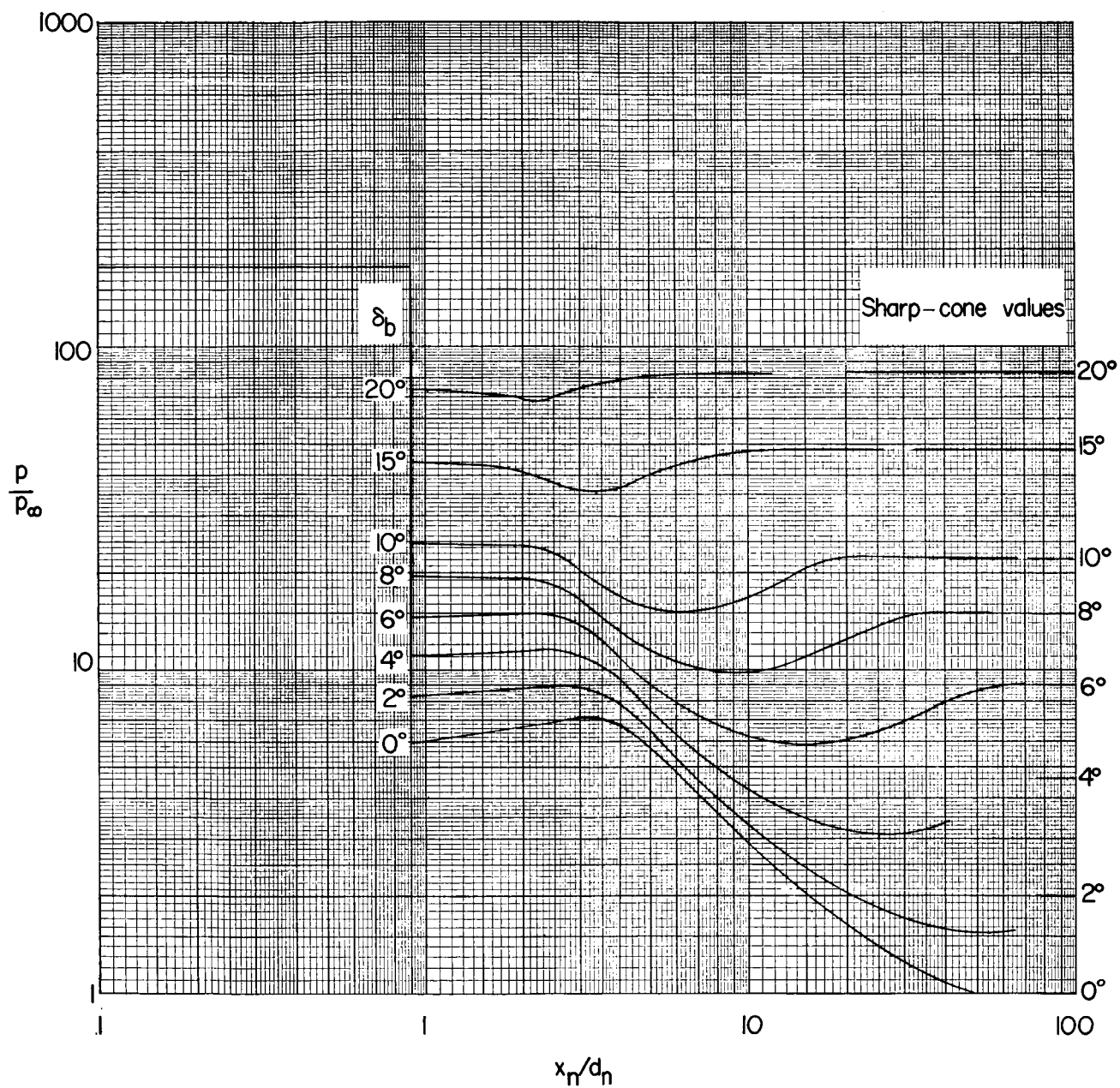


Figure 1.- Characteristics solutions for 30° forecone with various aftercones.
 $M_\infty = 19.8$; $\gamma = 5/3$.

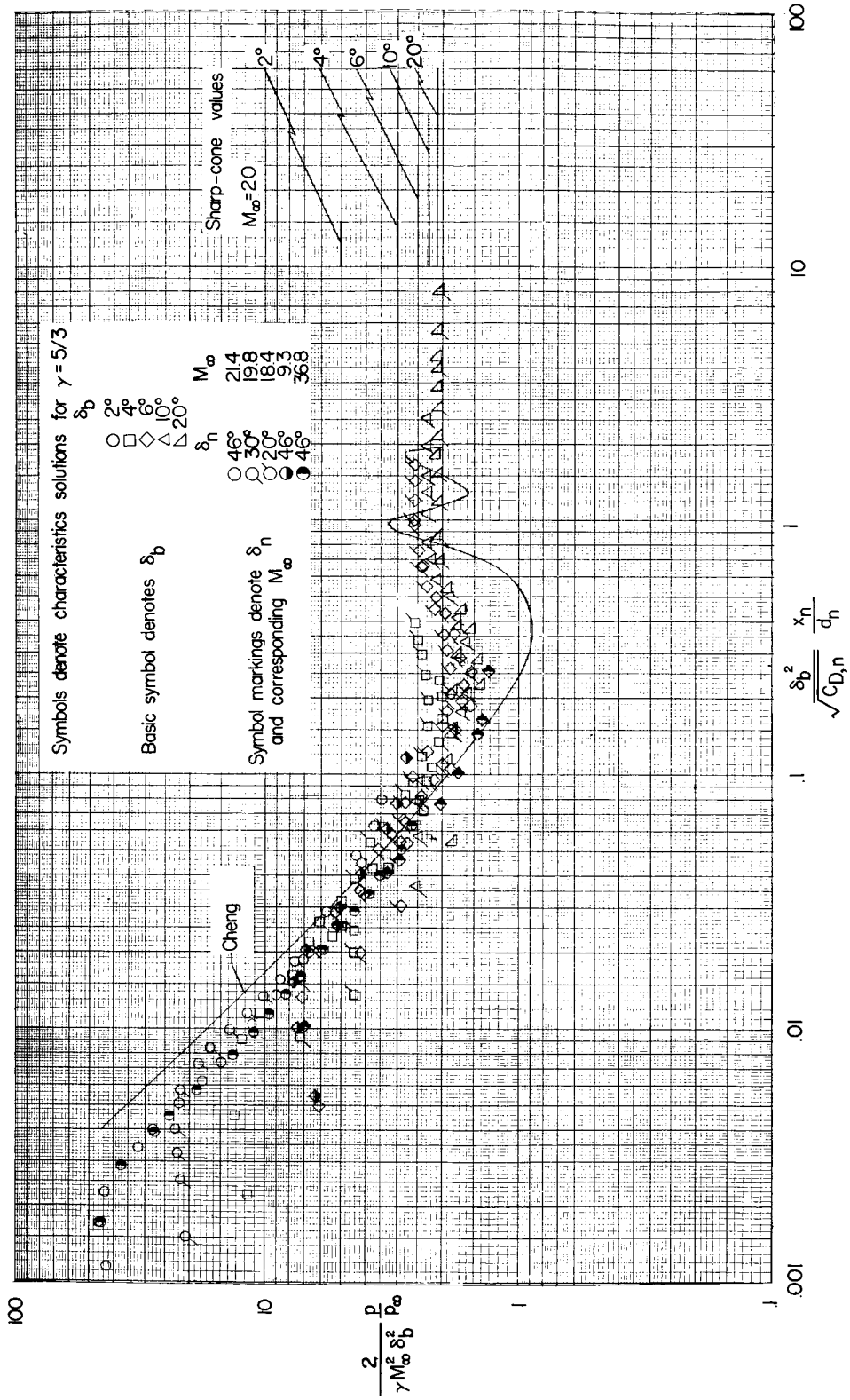
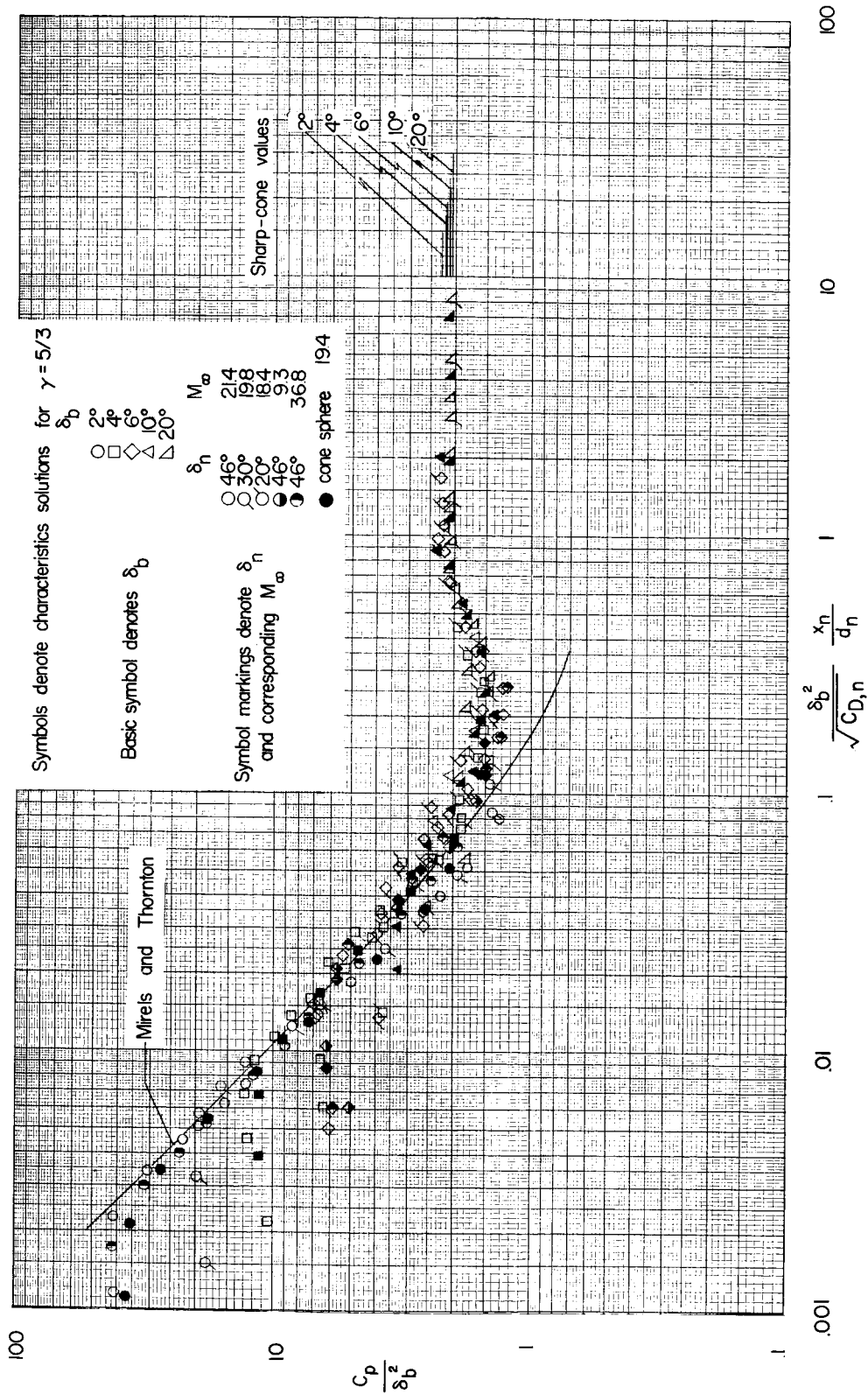


Figure 2.- Characteristics solutions of induced pressures in terms of correlating parameters developed by Cheng (ref. 2). $\gamma = 5/3$.



(a) Axial coordinate measured from nose tip.

Figure 3.- Characteristics solutions of induced pressures in terms of correlating parameters developed by Mirels and Thornton (ref. 3). $\gamma = 5/3$.

(b) Axial coordinate measured from forecone-aftercone junction.

Figure 3.- Concluded.

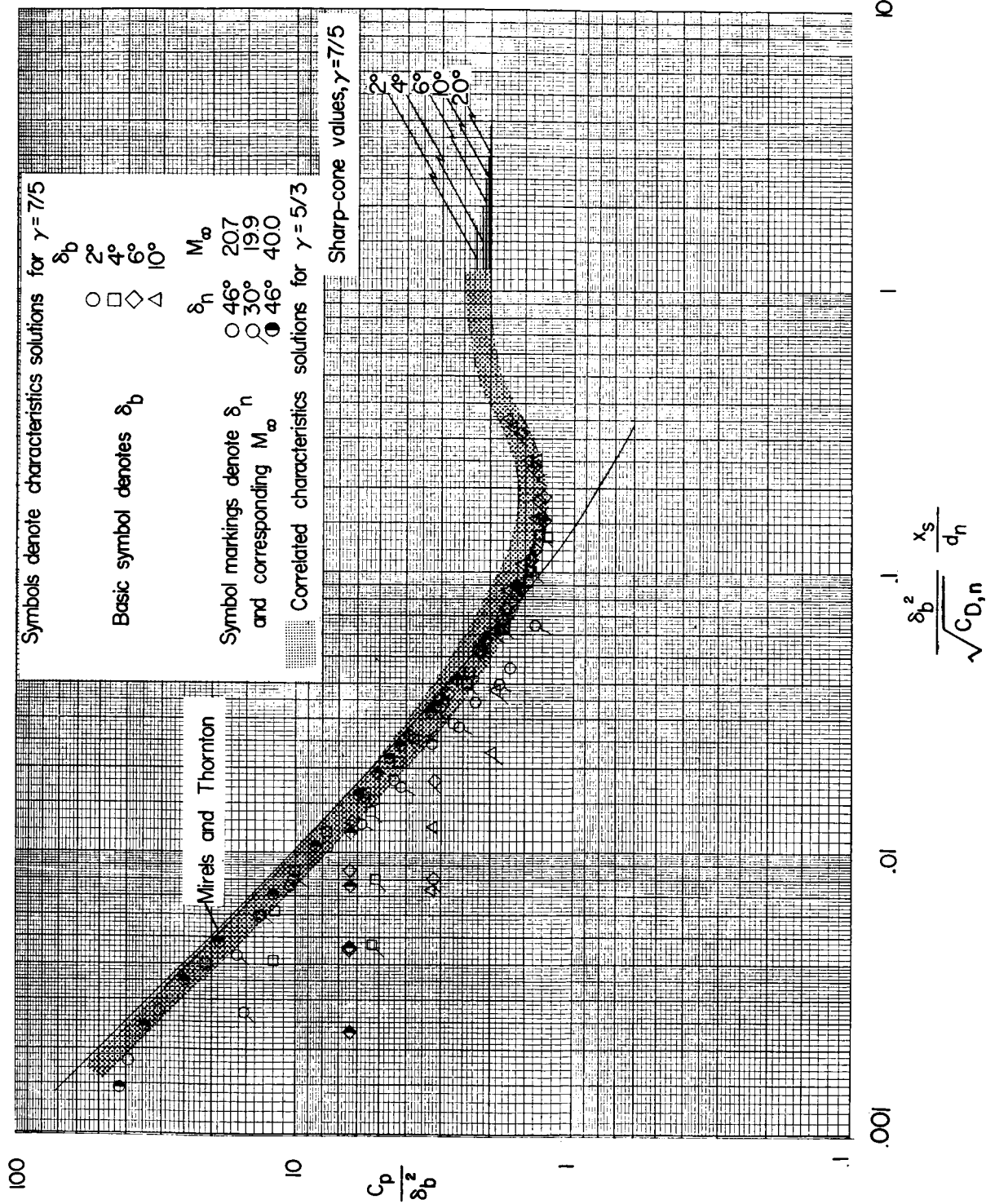
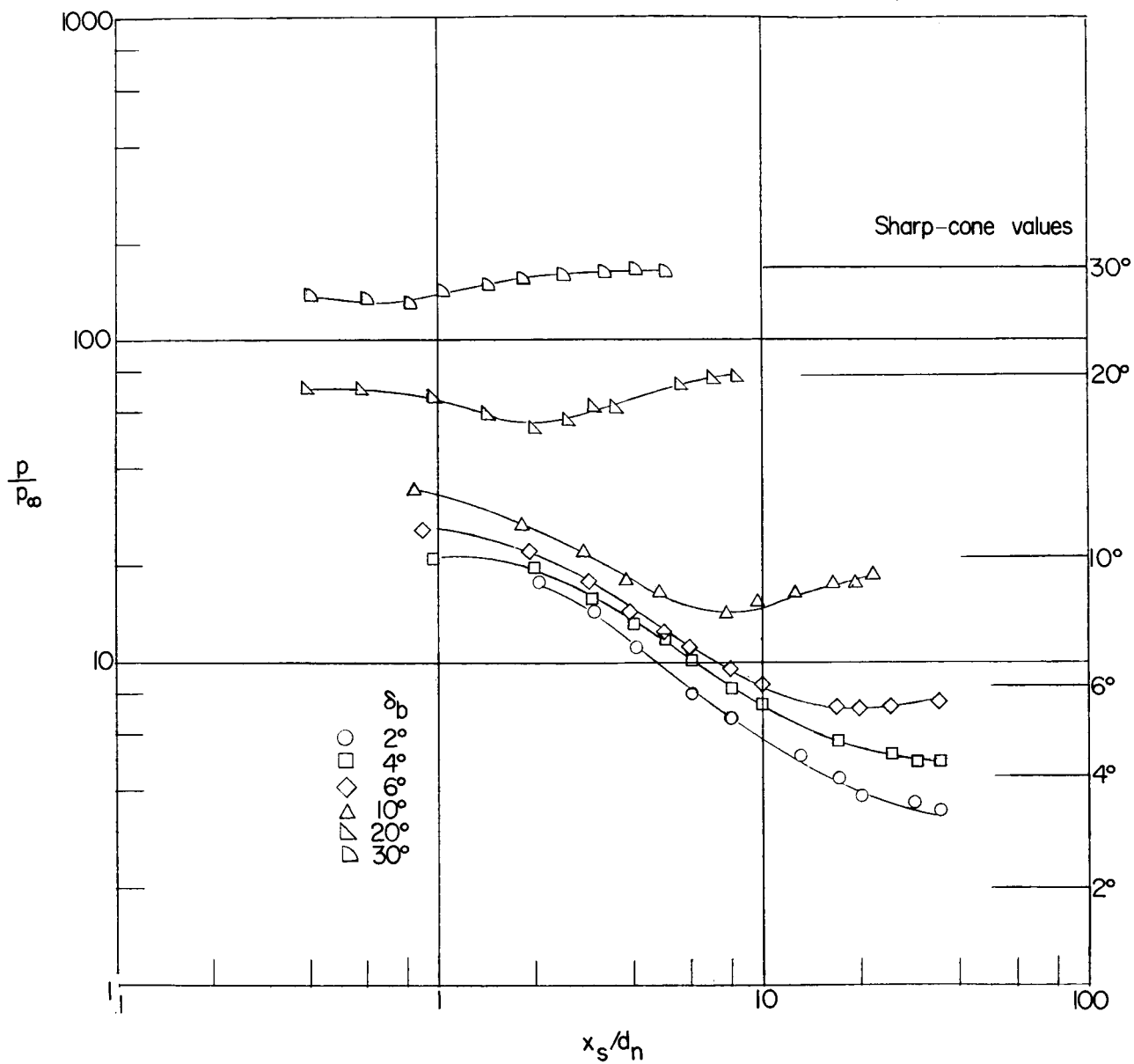
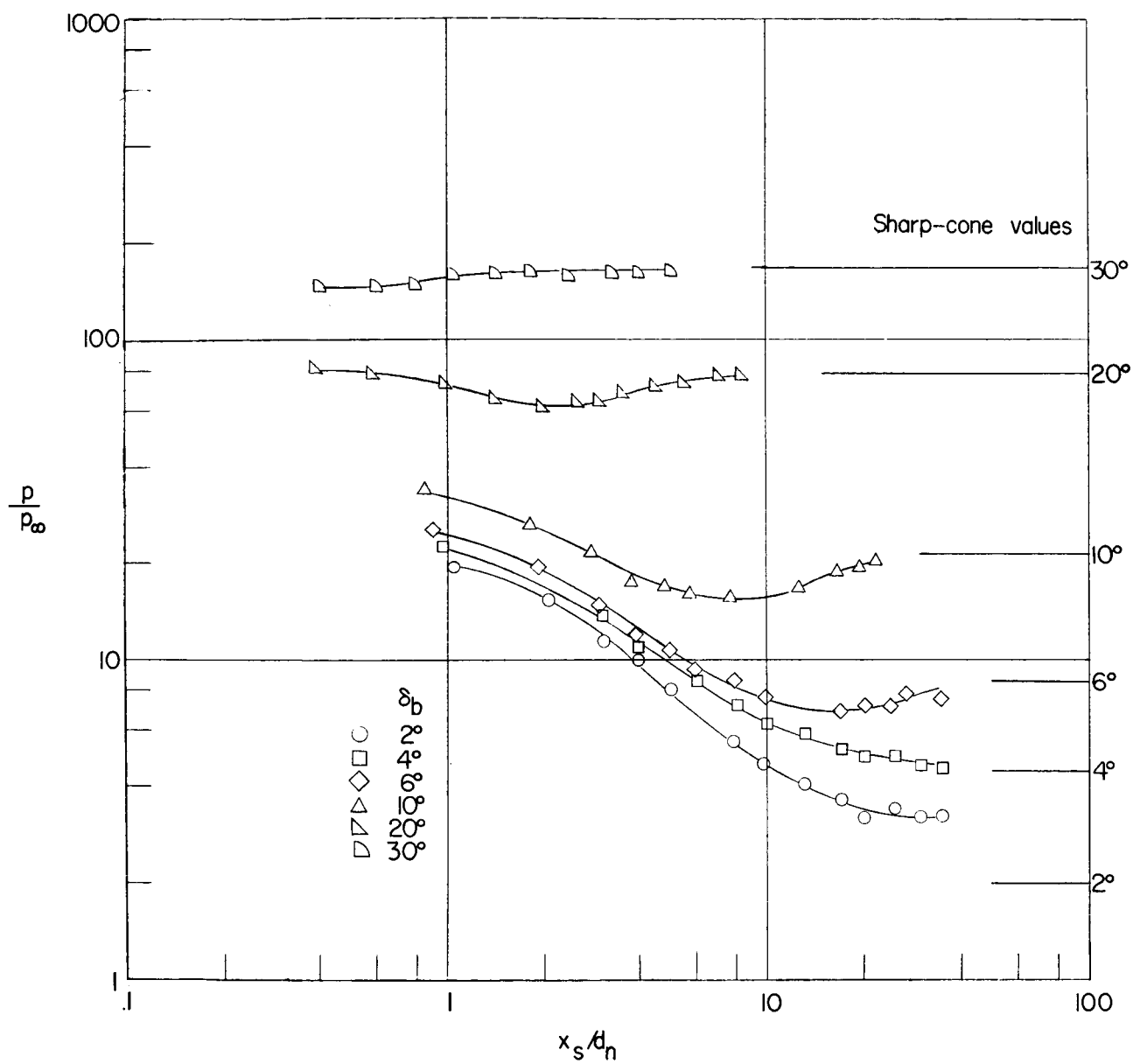


Figure 4.- Correlated characteristics solutions of induced pressures for $\gamma = 7/5$ compared with those for $\gamma = 5/3$.



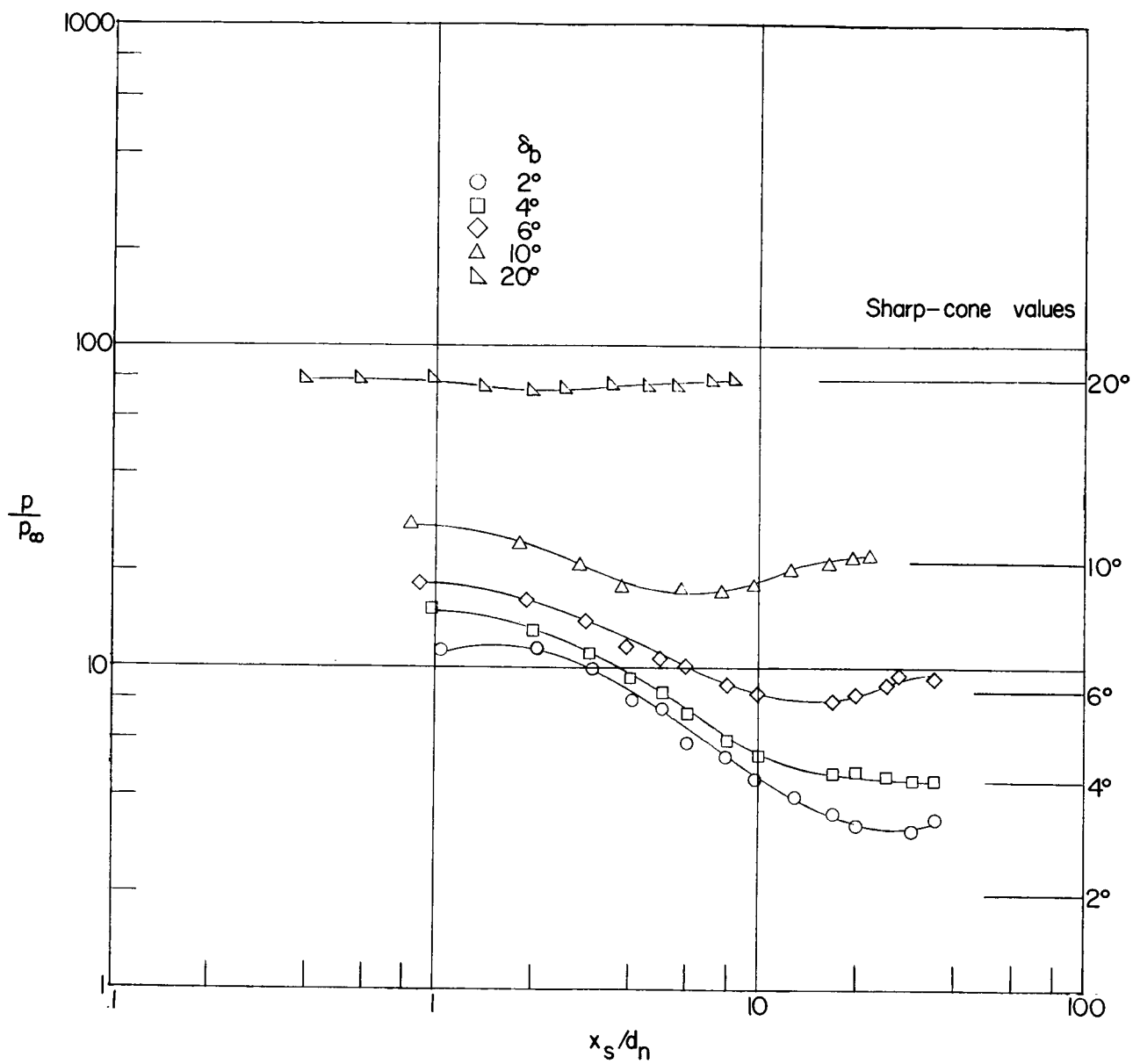
(a) 90° forecone.

Figure 5.- Experimental pressure distributions. $M_\infty = 19.4$; $R_{d,\infty} = 0.149 \times 10^6$.



(b) 46° forecone.

Figure 5.- Continued.



(c) 30° forecone.

Figure 5.- Concluded.

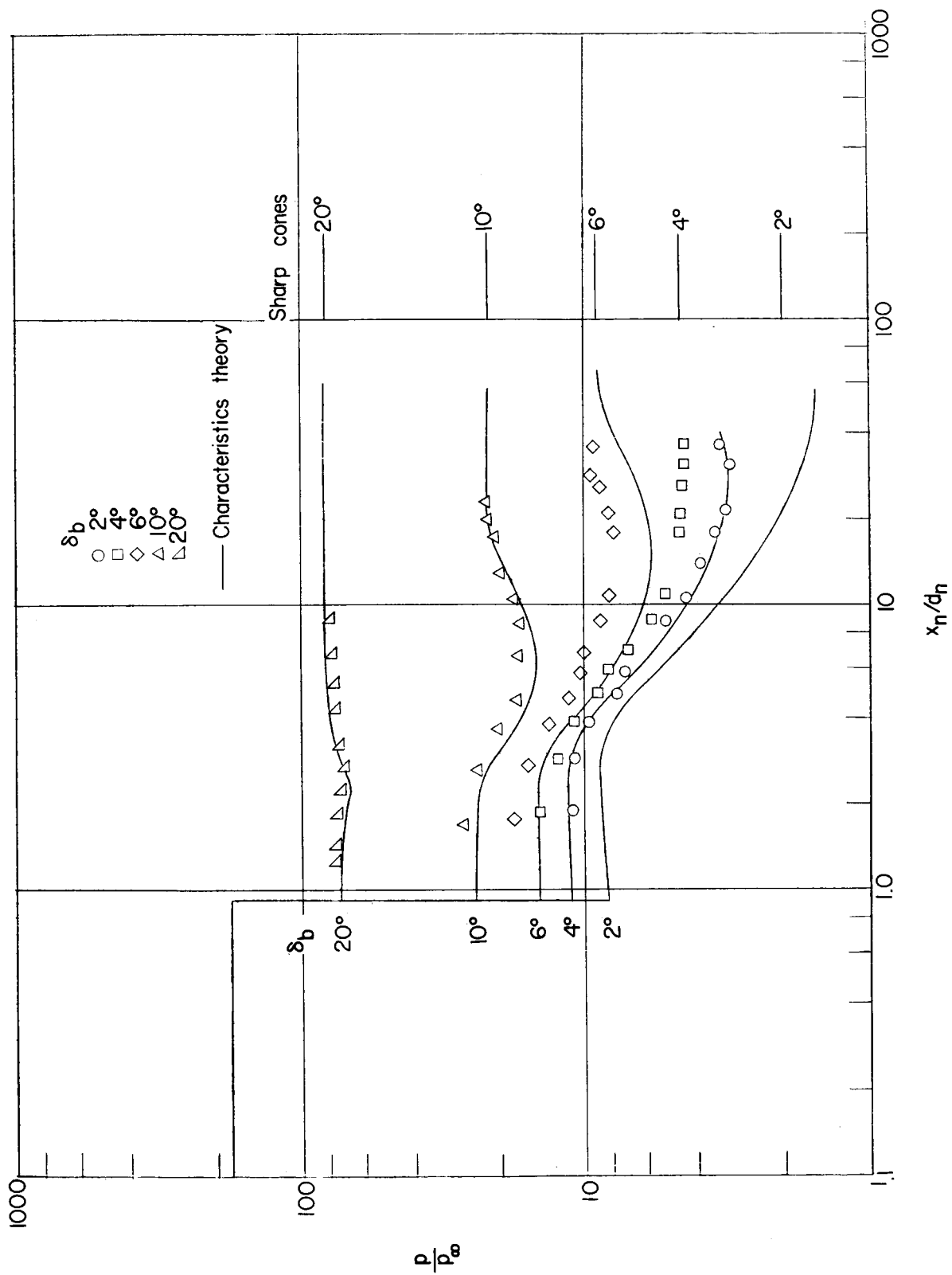


Figure 6.- Comparison of experimental pressures ($M_\infty = 19.4$; $R_{d,\infty} = 0.149 \times 10^6$) with exact inviscid solutions for 30° forecone. $\gamma = 5/3$.

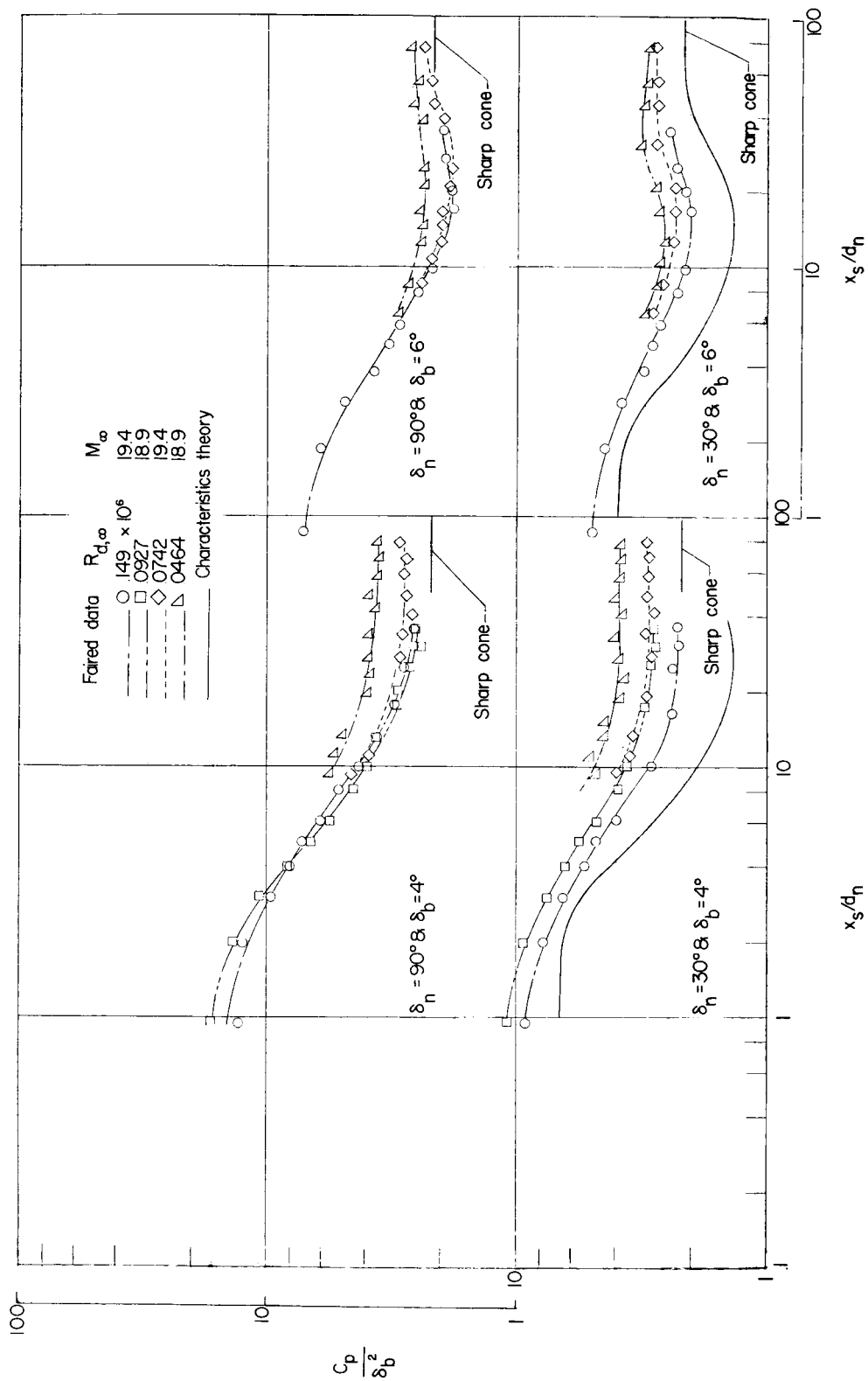


Figure 7.- Reynolds number effects on induced pressures.

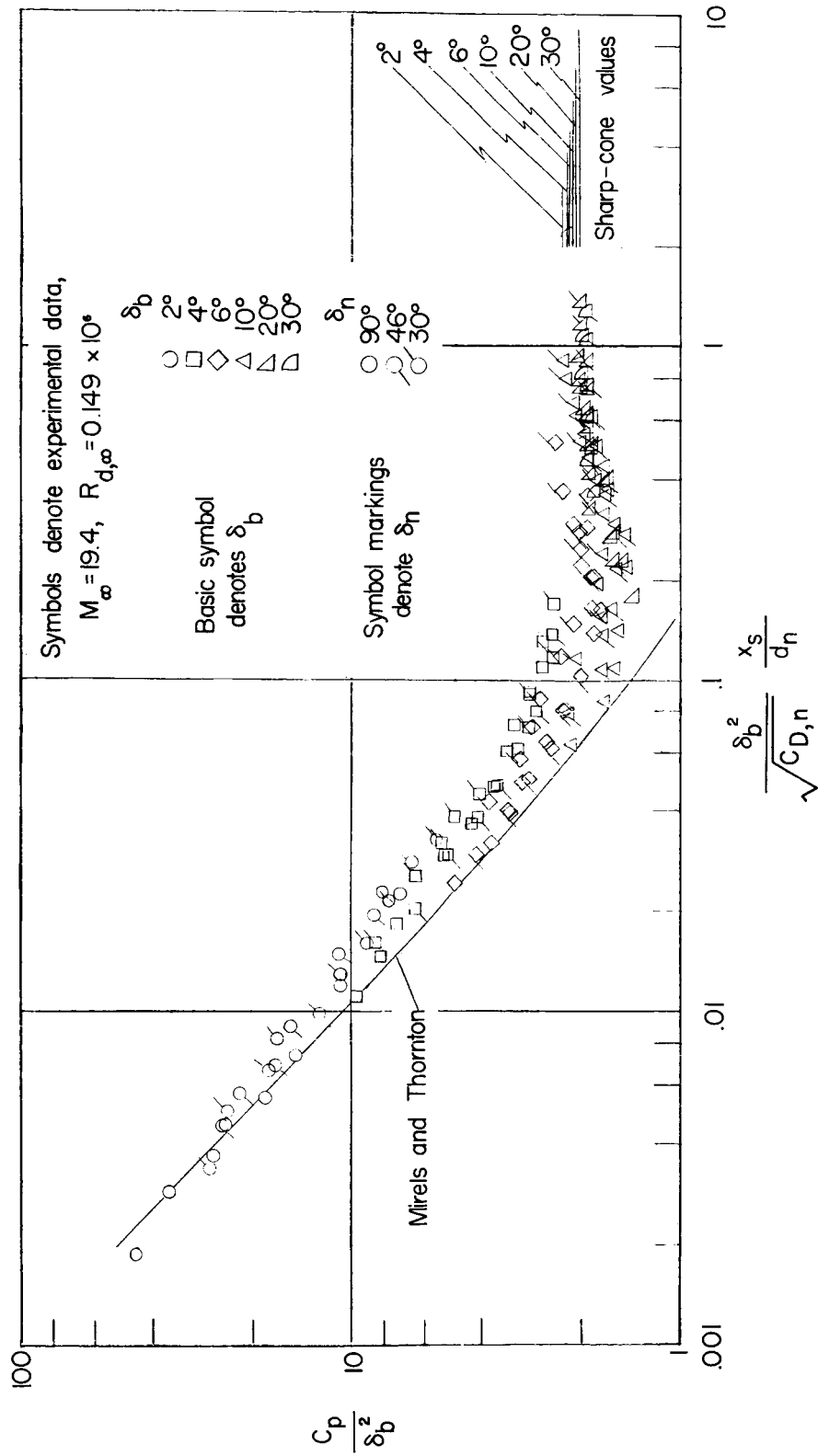


Figure 8.- Correlation of experimental induced pressures.

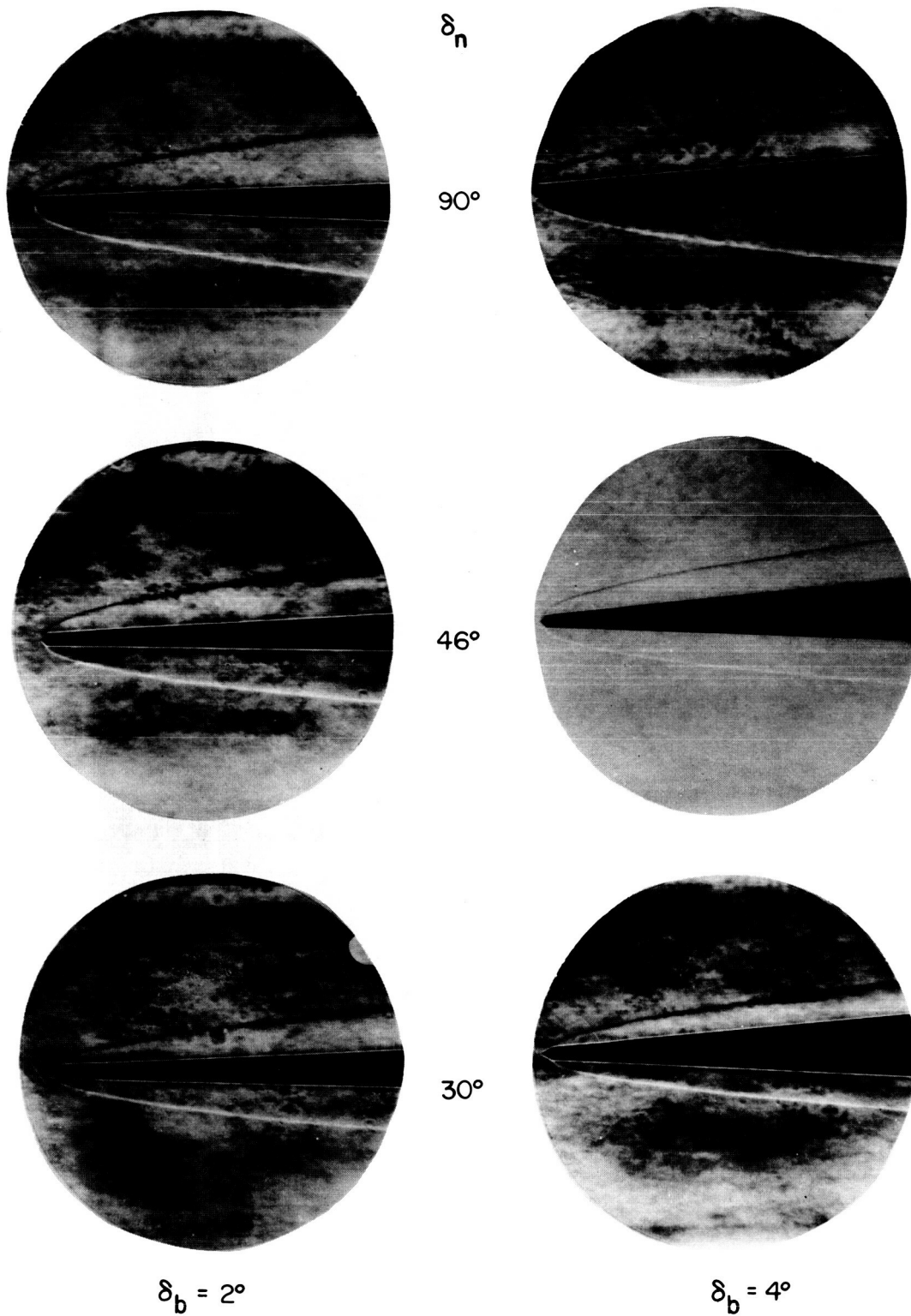
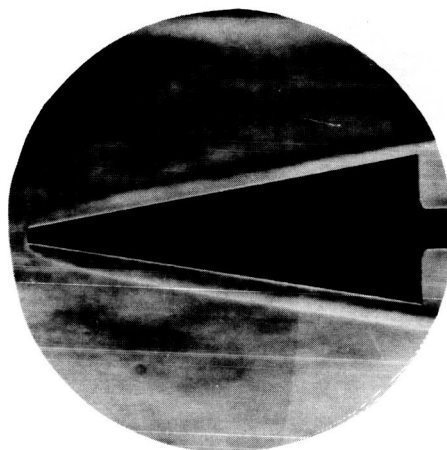


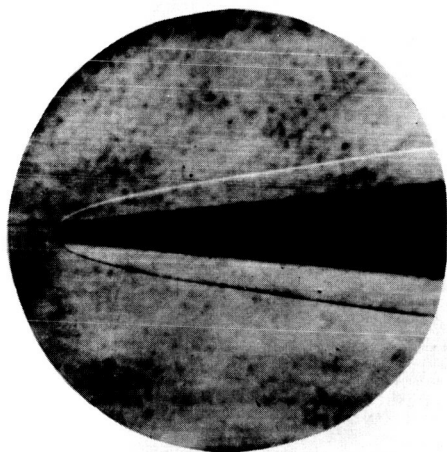
Figure 9.- Schlieren photographs showing shock shapes. $M_\infty = 19.4$; $R_{d,\infty} = 0.149 \times 10^6$. L-63-7524



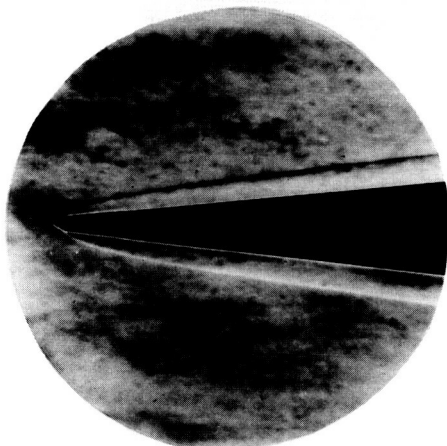
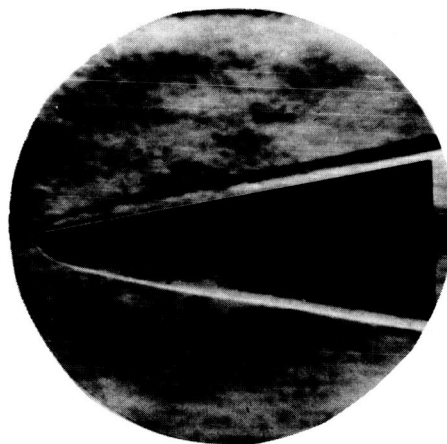
δ_n



90°



46°



$\delta_b = 6^\circ$

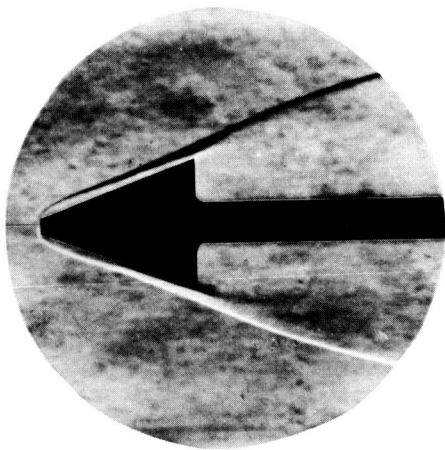
30°



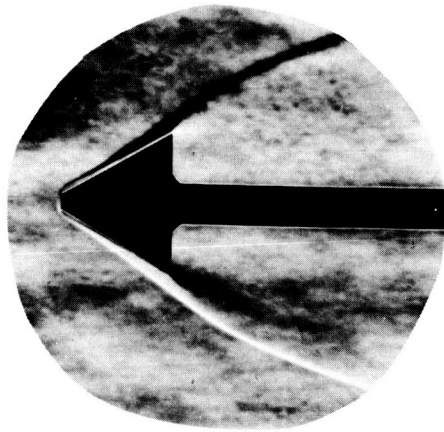
$\delta_b = 10^\circ$

Figure 9.- Continued.

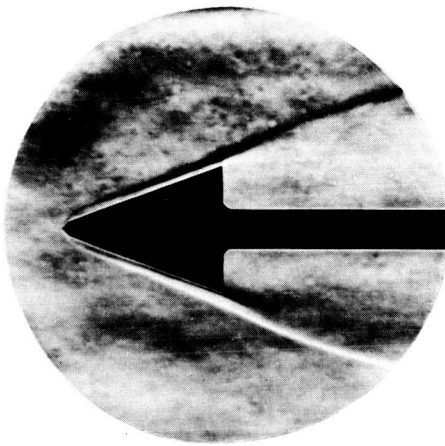
L-63-7525



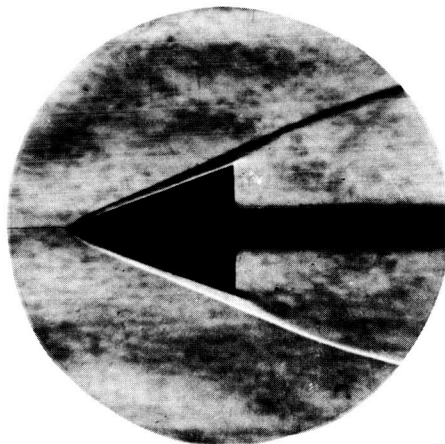
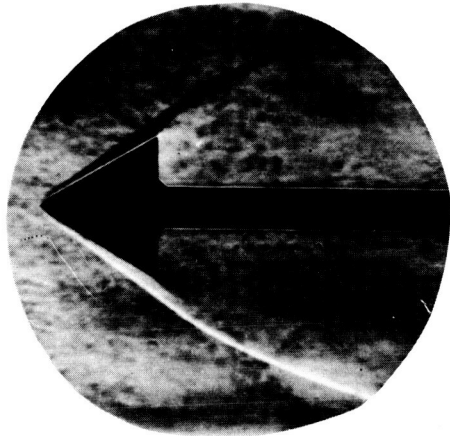
δ_n



90°



46°



30°

$\delta_b = 20^\circ$

$\delta_b = 30^\circ$

Figure 9.- Concluded.

L-63-7526

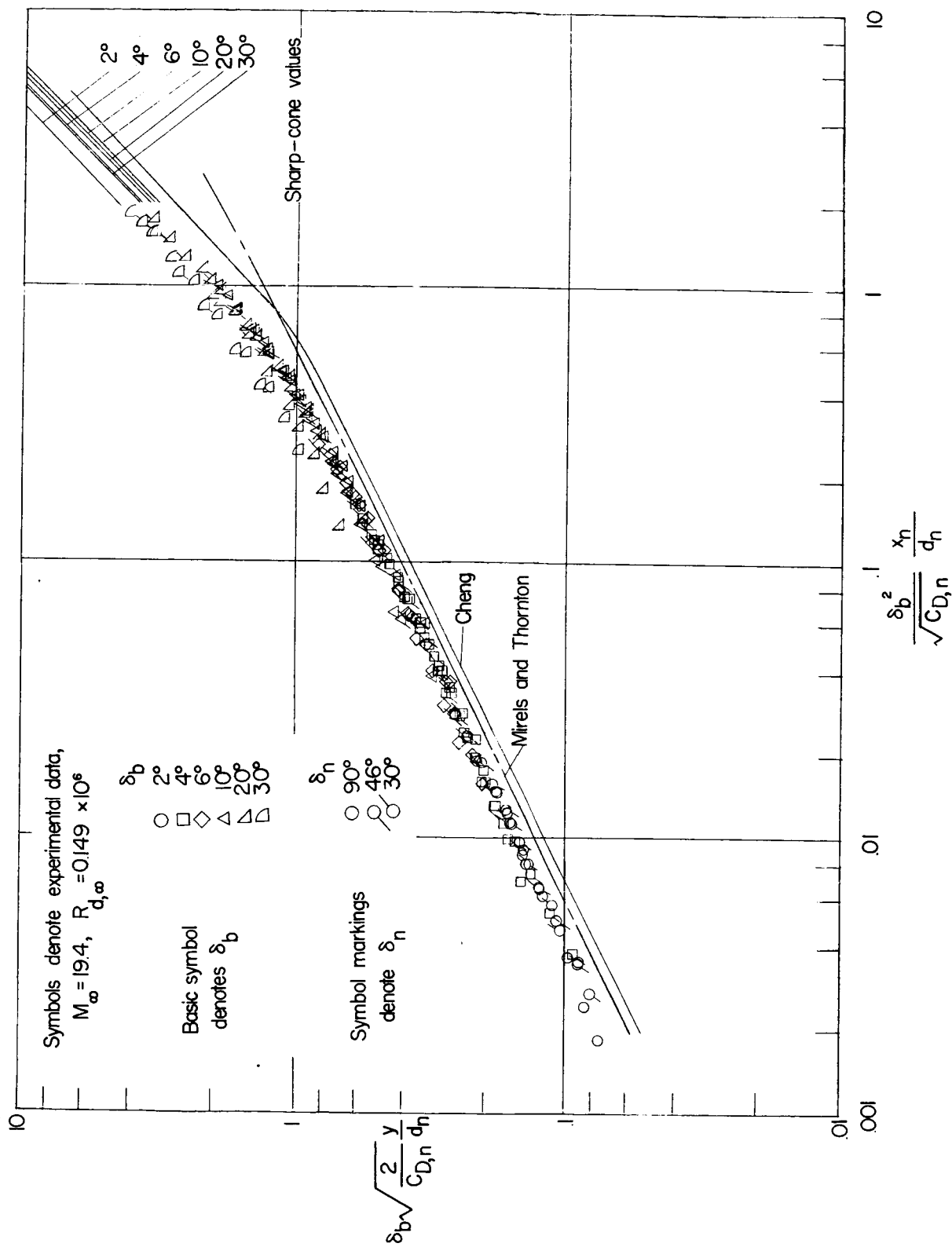


Figure 10.- Correlation of experimental shock shapes.